

See discussions, stats, and author profiles for this publication at: <https://www.researchgate.net/publication/281119072>

Striving Toward Noble-Metal-Free Photocatalytic Water Splitting: The Hydrogenated-Graphene-TiO₂ Prototype

ARTICLE in CHEMISTRY OF MATERIALS · AUGUST 2015

Impact Factor: 8.35 · DOI: 10.1021/acs.chemmater.5b02131

READS

93

11 AUTHORS, INCLUDING:



[Si Luo](#)
Brookhaven National Laboratory

8 PUBLICATIONS 21 CITATIONS

[SEE PROFILE](#)



[Eric Andrew Stach](#)
Brookhaven National Laboratory

392 PUBLICATIONS 15,718 CITATIONS

[SEE PROFILE](#)



[Sanjaya D. Senanayake](#)
Brookhaven National Laboratory

109 PUBLICATIONS 1,790 CITATIONS

[SEE PROFILE](#)



[Etsuko Fujita](#)
Brookhaven National Laboratory

175 PUBLICATIONS 5,375 CITATIONS

[SEE PROFILE](#)

Striving Toward Noble-Metal-Free Photocatalytic Water Splitting: The Hydrogenated-Graphene–TiO₂ Prototype

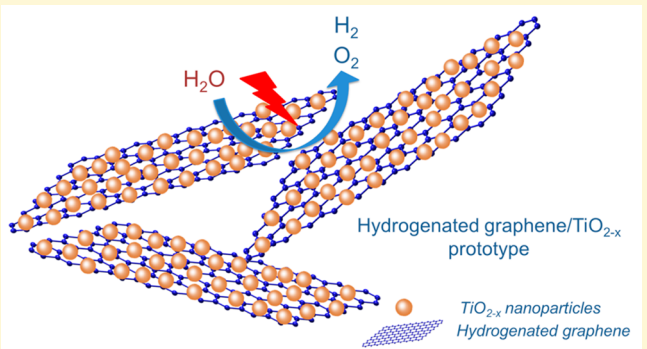
Thuy-Duong Nguyen-Phan,[†] Si Luo,^{†,‡} Zongyuan Liu,^{†,‡} Andrew D. Gamalski,[§] Jing Tao,^{||} Wenqian Xu,[†] Eric A. Stach,[§] Dmitry E. Poliansky,[†] Sanjaya D. Senanayake,[†] Etsuko Fujita,[†] and José A. Rodriguez*,[†]

[†]Chemistry Department, [§]Center for Functional Nanomaterials, and ^{||}Condensed Matter Physics and Materials Science Department, Brookhaven National Laboratory, Upton, New York 11973, United States

[‡]Department of Chemistry, Stony Brook University, Stony Brook, New York 11790, United States

Supporting Information

ABSTRACT: Graphane, graphene, and hydrogenated graphene (HG) have been extensively studied in recent years due to their interesting properties and potential use in commercial and industrial applications. The present study reports investigation of hydrogenated graphene/TiO_{2-x} (HGT) nanocomposites as photocatalysts for H₂ and O₂ production from water without the assistance of a noble metal cocatalyst. By combination of several techniques, the morphologies, bulk/atomic structure, and electronic properties of all the powders were exhaustively interrogated. Hydrogenation treatment efficiently reduces TiO₂ nanoparticles, while the graphene oxide sheets undergo the topotactic transformation from a graphene-like structure to a mixture of graphitic and turbostratic carbon (amorphous/disordered) upon altering the calcination atmosphere from a mildly reducing to a H₂-abundant environment. Remarkably, the hydrogenated graphene–TiO_{2-x} composite that results upon H₂-rich reduction exhibits the highest photocatalytic H₂ evolution performance equivalent to low loading of Pt (~0.12 wt %), whereas the addition of HG suppresses the O₂ production. We propose that such an enhancement can be attributed to a combination of factors including the introduction of oxygen vacancies and Ti³⁺ states, retarding the recombination of charge carriers, and thus, facilitating the charge transfer from TiO_{2-x} to the carbonaceous sheet.



INTRODUCTION

Since the discovery in 2004 by Novoselov et al.,^{1,2} graphene (GR), called the “mother of all graphitic forms”, has attracted considerable attention due to its unique structure, outstanding properties, and potential for use in commercial and industrial applications including electronics, mechanical devices, catalysis, and energy conversion. Tremendous efforts have been devoted to fabrication of the nanoassemblies of metal oxide and GR and its derivatives (graphene oxide—GO, reduced graphene oxide—RGO) for further potential applications.^{3–14} Among several systems containing a metal oxide and graphene, GR/TiO₂ composites have been reported to be highly promising, visible-light-responsive photocatalysts, active for processes such as wastewater treatment, air purification, solar water splitting, self-cleaning surfaces, and CO₂ reduction. The origin of such properties is largely due to simultaneously enhanced adsorption capacity, extended light absorption, superior stability, and excellent electron transport.^{15–30}

TiO₂ is the most widely used photocatalyst with a high propensity for generating pairs of electrons and holes upon photon absorption.^{31,32} A noteworthy obstacle is that both the rapid recombination of these charge carriers within nanoseconds and the limited absorption in the near-UV region

renders diminished either efficiency or activity of the photocatalytic reaction and partially limits its wide use in practical applications. The combination of TiO₂ with graphene efficiently overcomes these barriers due to its multifunction as an additional adsorbent, electron acceptor and transporter, stabilizer, and photosensitizer.^{15–30} GR sheets efficiently suppress the recombination of photoinduced electron–hole pairs, accelerate the transfer of electrons, and enhance the surface-adsorbed quantity of target molecules via π – π and electrostatic interactions, as well as extend the absorption range to the visible light region by either narrowing the band gap or introducing an additional gap.^{15–30}

Despite the fact that a cornucopia of scientific studies devoted to GR/TiO₂ composite materials has been reported, our fundamental understanding of these materials appears to have reached a plateau. Meanwhile, combining TiO₂ with fully hydrogenated graphene (known as “graphane”) or partially/half-hydrogenated graphene (as “graphone”) has not been achieved and remains at the forefront of photoelectrochemical

Received: May 22, 2015

Revised: August 20, 2015

Published: August 20, 2015

research. Graphane, graphene, or hydrogenated graphene (HG), where the GR's aromatic bonds are saturated with hydrogen atoms by high pressure hydrogenation, low pressure hydrogen plasma, and wet chemistry (Birch reduction), have been considered as promising semiconductor materials and as an efficient, stable support for anchoring metal/metal oxide catalysts.^{33–40} Due to the attachment of the atomic hydrogen to each site of the atomic scaffold of the GR lattice, the hybridization of carbon atoms alters the matrix from sp^2 to sp^3 , hence removing the conducting π -bands and opening an energy gap.³³ Upon hydrogenation of a honeycomb graphene lattice, three conformations of graphane can be generated, including chair, boat, and washboard conformations, and each conformer is characterized by a specific hydrogen sublattice and by a different buckling of the carbon sublattice.³⁵ The C–C bond lengths in graphane and graphene are different from that of graphene.^{34,35,37} Such HG materials exhibit ferromagnetism, and more importantly, its band gap is readily tunable, depending on the extent of hydrogenation. When half of the hydrogen in the graphane sheet is removed, the resulting semihydrogenated graphene or graphone becomes a ferromagnetic semiconductor with a small indirect gap arising from the formation of strong σ -bonds and the breakage of the delocalized π -bonding network of GR, leaving the electrons in the unhydrogenated carbon atoms localized and unpaired.³⁴ Notably, graphene is very different from graphane, with a large direct band gap, and also in comparison to GR, which has a zero band gap. Up to now, there are few experimental studies devoted to either graphane and graphone.^{33,36,39}

It is important to emphasize here that the introduction of hydrogen species by either physical or chemical methods not only successfully produces such a GR-like family of materials but also imparts a modification to the reduced titania (TiO_{2-x}) with a substoichiometric Ti:O ratio. The coloration of TiO_2 (red, yellow, blue, gray, black) has sparked increasing research interest in recent years with the promise of overcoming the challenges of purely white TiO_2 itself.^{41–46} The synthesis and functionality of such nanomaterials have been a very promising approach, not only to drastically enhance the activity by increasing the quantum efficiency but also to extend the optical absorption into the visible region by introducing a substantial amount of lattice disorder or defects.^{41–43}

In the light of these facts, investigating the hydrogen coverage via the extent of hydrogenation, on the coupling of TiO_{2-x} with hydrogenated graphene, graphone, or graphane, is a promising approach that possibly exhibits strong impact on the structural, physicochemical, optical, and electronic characteristics and even the catalytic activity of these materials. Wang et al.⁴⁷ synthesized hydrogenated TiO_2 -RGO via the hydrogenation of TiO_2 –graphite oxide at 450 °C for 4 h under a flowing atmosphere of 5% H₂/95% Ar. Such a composite was used as anode material in a high rate lithium ion battery, achieving a larger discharge capacity (234.3 mA h g⁻¹) than the composite reduced by hydrazine, and was subsequently annealed in nitrogen atmosphere. Much higher reversible discharge capacity at a current rate of 5 C (up to 166.3 mA h g⁻¹), remarkable rate capability, and outstanding cycling stability (2.4% capacity loss after 100 cycles) are attributed to the greatly improved electronic conductivity derived from hydrogenated TiO_2 (H-TiO₂), enhanced electron transport due to the role of reduced graphene as a conductive substrate, and the good contact between the zero-dimensional H-TiO₂ nanoparticles with two-dimensional (2D) RGO nanosheets.

Very recently, Zhang and Chen⁴⁸ reported the influence of hydrogenation temperature for GO-TiO₂ composites on the photocatalytic degradation of Rhodamine B. The highest photocatalytic activity was obtained by the hybrid material prepared at 450 °C due to the formation of p–n junctions and appropriate charge mobility.

Given these many aspects, we have endeavored to systematically investigate in this study the influence of hydrogenation extent on the structural, physicochemical, and electronic properties of hydrothermal-prepared GO-TiO₂ composites. The impact of this structure on the light-driven O₂ and H₂ production from water without the assistance of noble metal cocatalyst (i.e., Pt, Ru, Rh) was interrogated and the role of individual components in the overall photocatalytic reaction was proposed. Otherwise, one should bear in mind that due to the high cost and frequent scarcity of Pt in Earth's crust, its use has been strictly controlled, and herein, hydrogenated graphene–TiO_{2-x} composites were benchmarked against the well-known Pt/TiO₂ system, demonstrating the potential of new noble-metal-free catalysts to replace expensive and nonabundant metals in terms of economics, abundance, environmental considerations, and catalytic effectiveness.

■ EXPERIMENTAL SECTION

Synthesis of Materials. The GO dispersion (3.5 mg mL⁻¹) was synthesized by a modified Hummers method, and the detailed preparation is described in the [Supporting Information](#). In a typical procedure, 7 mL of titanium *n*-butoxide and 1 mL of hydrochloric acid (35 wt %) were loaded into a Teflon-lined stainless steel autoclave and statically aged at 150 °C for 6 h. After cooling to room temperature, the white precipitate was washed by ethanol and centrifuged at 15 000 rpm and redispersed into ethanol. The *as-syn* TiO₂ was obtained by freeze-drying the product after washing and centrifugation. A desired amount of GO dispersion (1 wt %) was added into the TiO₂–ethanol dispersion under vigorous stirring at room temperature for 30 min. After sonicating for 30 min, the mixture was hydrothermally treated at 80 °C for 4 h. Subsequent to washing with deionized water, the product was lyophilized and hydrogenated at 500 °C for 4 h. The final composites were then annealed in two environments: (i) hydrogen–argon mixture (15% H₂/85% Ar) and (ii) ultrahigh-purity H₂, denoted as HGT@H₂/Ar and HGT@H₂, respectively.

For comparison, hydrogen-reduced titania was also prepared by the same procedure without the addition of GO and named as TiO_{2-x}@H₂. Other control samples include nanosized anatase calcined in ambient air (TiO₂) and GO annealed in pure H₂ (HG@H₂).

Characterizations. X-ray diffraction (XRD) patterns and pair distribution function (PDF) profiles were collected at beamline X7B ($\lambda = 0.3196 \text{ \AA}$) of the National Synchrotron Light Source (NSLS) at Brookhaven National Laboratory (BNL). The powder samples (5 mg) were loaded into a 0.9 mm-ID quartz capillary, and the two-dimensional diffraction patterns were collected by a PerkinElmer amorphous silicon detector. The raw data were integrated by Fit2D code (calibrated by LaB₆ standard) while the crystalline phase identification, composition, and lattice parameters were subsequently analyzed by Rietveld refinement using the General Structure Analysis System (GSAS) program. PDF data processing was subsequently performed with Python/PDFgetX3 to describe the distribution of all pairs of atoms within a sample as a function of interatomic distance.

High-resolution X-ray photoemission spectra were collected at beamline U12A of the NSLS at BNL examining the Ti 2p, C 1s, and O 1s core level regions. The probing depth for 700 eV-photon energy was 8 nm, and the data were further processed by CASAXPS.

Further characterization of the materials was also conducted using several techniques available at the Center for Functional Nanomaterials (CFN) at BNL. Scanning electron microscopy (SEM) was carried out by a Hitachi S-4800. Transmission electron microscopy (TEM) images were recorded on a FEI Titan 80-300 with an objective-lens

aberration corrector and a field-emission gun operating at 300 kV. The powder samples were dispersed in water by sonication and dropped onto a carbon film coated copper grid and air-dried overnight. Raman spectroscopy was performed on WiTec Alpha combination microscope at room temperature with 633 nm laser as an excitation source. UV-vis diffuse reflectance (DRS) measurements were collected at room temperature by PerkinElmer Lambda 950 spectrometer equipped with an integrating sphere assembly.

Brunauer–Emmett–Teller (BET) specific surface areas were determined by N₂ adsorption/desorption at 77 K using an Altimira AMI-300ip instrument. The powders were degassed at 150 °C to remove all surface-adsorbed contaminants prior to measurements. Solid state ¹H nuclear magnetic resonance (NMR) spectroscopy was conducted on a Bruker Advance III, operating at 500 MHz at room temperature. The magic angle spinning (MAS) frequency was 12 kHz and one-dimensional spectra were acquired with 16 scans. ¹H chemical shifts were externally referenced to adamantane, and NMR data were further processed using TopSpin 3.1.

Photocatalytic Water Splitting Measurements. The photocatalytic water splitting activity was evaluated through the measurement of either hydrogen or oxygen evolution in a closed gas circulation and evacuation system. The aqueous methanol solution (20 vol %) and 0.01 M AgNO₃ were used as sacrificial agents to probe the H₂ and O₂ gas evolution, respectively, in separate experiments. The reactor was side-irradiated by a 150 W Xe arc lamp from Optical Building Blocks Corporation which utilizes elliptical reflector ($F = 379$ mm) and was equipped with CuSO₄ filter (310 nm < λ < 625 nm, see in Figure S1—*Supporting Information*). The lamp was placed in the focal point of the lamp, and the light intensity was 750 mW over an irradiated area of 1.13 cm², which was measured by an optical power meter (Ophir Optronics). A 400 nm long pass filter (Thorlabs, Inc.) was used to measure the activity under visible light illumination (light intensity 475 mW, 400 nm < λ < 625 nm). The detailed experimental conditions and procedures can be found in a previous study.⁴⁹ The evolved gases were determined by gas chromatography (GC Agilent 6890N) equipped with FID and TCD detectors using Ar as the carrier gas. The apparent quantum efficiency (QE) was calculated according to the following equation (Table S1 in *Supporting Information*):

$$\text{QE [\%]} = \frac{\text{number of reacted electrons}}{\text{number of incident photons}} \times 100 \\ = \frac{\text{number of evolved H}_2 \text{ molecules} \times 2}{\text{number of incident photons}} \times 100$$

■ RESULTS AND DISCUSSION

Structural Studies—XRD, PDF, Raman, and ¹H NMR.

The *as-syn* GO–TiO₂ composite was subsequently annealed at 500 °C for 4 h in two different atmospheres: (i) flow of 15% H₂ in Ar and (ii) ultrahigh-purity H₂ (both under 20 psi), to investigate the effectiveness of hydrogenation on the structural, physicochemical, and electronic properties and photocatalytic performance. The specific surface areas of all samples measured by N₂ sorption are shown in Table 1. The content of HG in the composites after H₂ reduction was determined by thermogravimetric (TGA) analysis under air flow, ~0.8 wt % (depicted in Figure S2, *Supporting Information*). The crystallographic structures of HGT composites and other reference materials were confirmed by synchrotron XRD patterns displayed in Figure 1A. In all samples, a series of well-defined (101), (004), (200), (105), (211), and (204) diffraction peaks are indexed to the tetragonal anatase (space group $I4_1/AMD$) without any trace of rutile. Herein, the crystallinity decreases due to the evolvement of hydrogen gas, leading to the formation of defects that inhibit the crystal growth of TiO_{2-x}, except for HGT@H₂. Notably, a lack of diffraction peaks representative of the carbonaceous component can possibly be explained by the

Table 1. Textural and Structural Parameters

samples	surface area, ^a m ² g ⁻¹	crystallite size, ^b nm	lattice parameters, ^b Å		peak intensity ratio I _D /I _G ^c
			a = b	c	
TiO ₂	47.5	14.19	3.7858	9.5106	-
TiO _{2-x} @H ₂	56.6	13.10	3.7855	9.5089	-
HGT@H ₂ /Ar	123.3	9.17	3.7877	9.5100	1.53
HGT@H ₂	74.9	12.10	3.7885	9.5165	1.26

^aFrom N₂ sorption. ^bFrom XRD. ^cFrom Raman analyses.

exfoliation of GO nanosheets during synthesis, the intercalation of TiO₂ particles, or the shielding of the (002) carbon-like feature by the strong (101) diffraction of anatase TiO₂.^{15,16,19,22} The crystalline phase, particle size, and unit cell parameters were determined by Rietveld refinement and are summarized in Table 1. As seen in Figure S3 (*Supporting Information*) and Table 1, annealing in an H₂ atmosphere clearly causes a lattice distortion in both TiO_{2-x}@H₂ and HGT composites. Particularly, a lattice expansion is found on HGT composites whereas the shrinkage occurs on TiO_{2-x}@H₂. The average crystallite size remarkably increases from 6 nm (*as-syn* TiO₂) to 9–13 nm under a reducing atmosphere compared to TiO₂ (14 nm). It can be seen that the lack of oxygen in the H₂-reducing environment efficiently aggravates the deformation of the unit cell and restrains the grain growth during calcination.

In addition, the PDF signal takes into account all components of the XRD pattern and contains all characteristic interatomic distances in the materials. The corresponding PDF profile in Figure 1B points to numerous well-defined maxima at 1.96, 2.39, and 3.05 Å that are ascribable to the mean bond lengths of Ti–O, O–O, and Ti–Ti pairs for the first neighbor coordination shell of [TiO₆] octahedra (the closest O shell around a Ti atom). Note that each Ti ion in the anatase structure octahedrally coordinates to six O ions with an atypical Ti–O bond length of 1.98 Å and an equatorial bond length of 1.93 Å.⁵⁰ The peaks at 3.83 Å represent the second asymmetric Ti–Ti,O coordination sphere. No apparent differences are encountered among these samples except the shift to a larger interatomic distance and the alteration in maxima intensity upon hydrogenation, implying the distortion of [TiO₆] octahedra. Apart from the distances less than 6 Å—considerable short- and medium-range order—the longer correlation up to 20 Å in Figure S4 (*Supporting Information*) clearly demonstrates the absence of long-range order, indicating the surface disorder or structural distortion by hydrogenation.

Raman spectroscopy, a nondestructive method, is also a useful technique to explore the crystalline or molecular changes after hydrogenation via molecular vibrations. Figure 1C shows several characteristic Raman-active modes at 145 (E_g), 198 (E_g), 398 (B_{1g}), 516 (A_{1g} + B_{1g}), and 638 (E_g) cm⁻¹ for TiO₂, identifying the tetragonal structure of anatase TiO₂ which is consistent with XRD observations. These modes become weakened and broaden together with the emerging of numerous smaller, weaker bands for either TiO_{2-x}@H₂ or HGT composites after H₂ reduction, stemming most likely from the surface heterogeneity or disorder that may activate zone-edge and otherwise Raman-forbidden modes by breaking down the Raman selection rules.^{41,51} The results in our study are consistent with previous reports which claim that the introduction of H₂ induced the spreading and impairment of

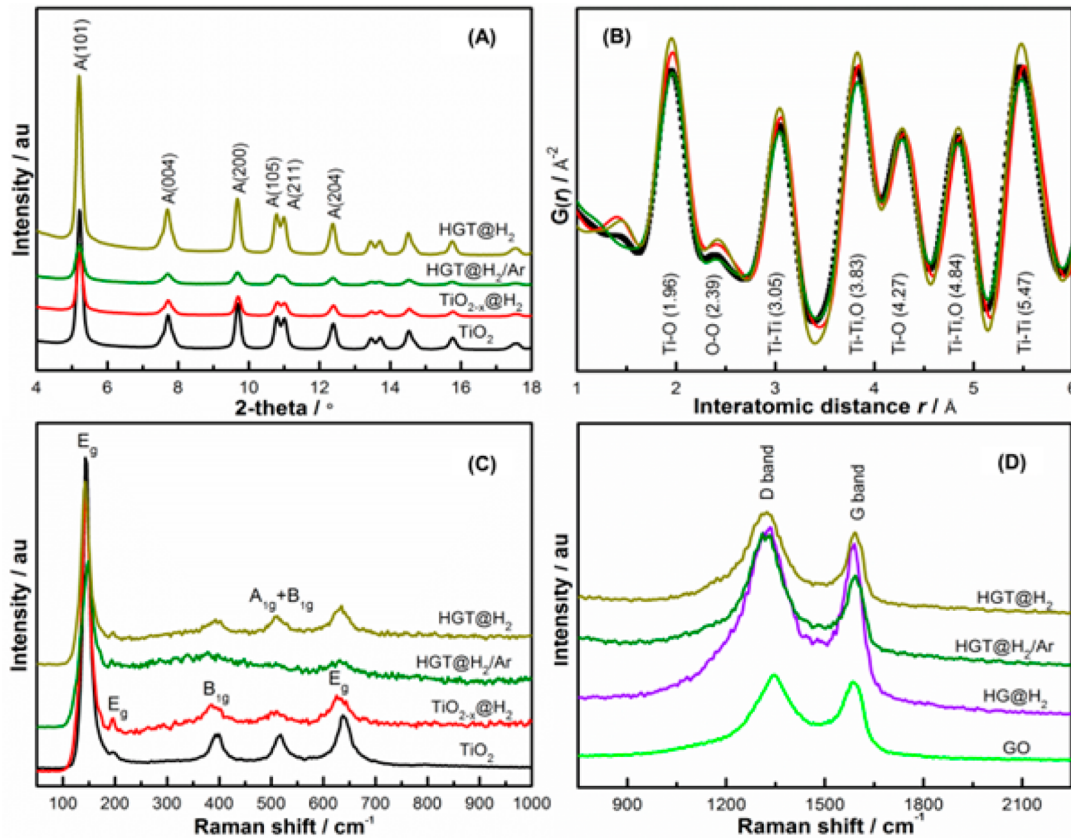


Figure 1. (A) XRD patterns, (B) PDF analysis, and (C, D) Raman spectra of TiO_2 , $\text{TiO}_{2-x}@\text{H}_2$, and HGT composites.

these indicative bands, implicating hydrogenation-induced structural changes at the surface.^{41–43} Moreover, the formation of intrinsic defects is one of the possible reasons for Raman mode broadening because as they scatter phonons, causing their decay and consequent decrease in their lifetime, it results in an increase in the phonon line width.^{52,53}

Raman spectroscopy can also be utilized to identify either sp^2-sp^3 hybridized carbon atoms or disorder/defects in HG composites. As illustrated in Figure 1D, two typical D and G bands are observed in both samples. The D band at 1350 cm^{-1} is assigned to the vibration of carbon atoms with the sp^3 electronic configuration of disordered graphene or sp^3 defects near the K-point, whereas the G band at 1587 cm^{-1} is associated with the in-plane vibration of sp^2 -bonded carbon atoms at the Γ -point and a doubly degenerated phonon mode (E_{2g} symmetry) at the Brillouin zone center.^{18,54,55} The relative intensity ratio (I_D/I_G) is usually calculated to provide the information on the relative concentration of disorder or local defects in comparison with sp^2 -hybridized graphene domains. The $I_D/I_G = 1.12$ of HG annealed in H_2 is slightly higher than that of the GO precursor ($I_D/I_G = 1.05$), indicating a substantial decrease in sp^2 -bonded carbon atoms and oxidized molecular defects.⁵⁵ It is noteworthy that the integrated intensity significantly increases to 1.51 and 1.26 for HGT@ H_2/Ar and HGT@ H_2 , demonstrating the formation of large amounts of edges, defects, and disorders as well as abundant sp^3 C–H bonds and dense ripples after hydrogenation.⁵⁶ Interestingly, weaker signals are recorded for HGT@ H_2 , indicating the lower portion of graphitic structure or lower graphitization degree compared to HGT@ H_2/Ar . The nature of the carbonaceous

component was further investigated by TEM and XPS in the following section.

The solid state ^1H NMR spectroscopy was further conducted to characterize the hydrogen-containing species in the TiO_2 , $\text{TiO}_{2-x}@\text{H}_2$, and HGT composites (Figure 2). The chemical shifts of all resonances are shown in Table 2. A strong, sharp chemical shift at 5.63 ppm (resonance A) and very small peak at 1.18 ppm (resonance B) in TiO_2 are characteristic of the H at bridging and terminal sites.⁵⁷ Chary et al.⁵⁸ ascribed the low field peak to acidic OH groups coordinated to two Ti atoms, localized on bridging oxygen atoms and forming weak hydrogen bond adjacent to oxygen atoms, while the high field peak belongs to basic OH groups where hydrogen atoms are bound to terminal oxygen atoms. According to Jonsen,⁵⁹ the sharp, small, and narrow resonance implies that the hydrogen concentration is relatively low and these hydrogen species are situated in dynamically static and isolated interstitial sites within the oxide lattice. Otherwise, the broad signal involves hydroxyl protons and labile interstitial protons (surface and/or bulk), which experiencing extensive dynamic averaging. The shifting toward lower field and line width broadening of these signals are obvious for $\text{TiO}_{2-x}@\text{H}_2$ while the signal of terminal Ti–OH drastically increases. Two additional resonances at 3.68 (C) and 0.28 ppm (D) can be reasonably attributed to titanol groups located at internal defect sites.⁵⁷ These groups can be ascribed to the H located in the disordered phase upon hydrogenation.^{43,44} Annealing the HGT composite under two different environments induces different surface hydroxy/hydroxylated species: H_2/Ar mixture gives a strong, broad resonance at 5.49 ppm, and a sharp, small one at 0.38 ppm whereas three intense resonances at 5.35, 3.44, and

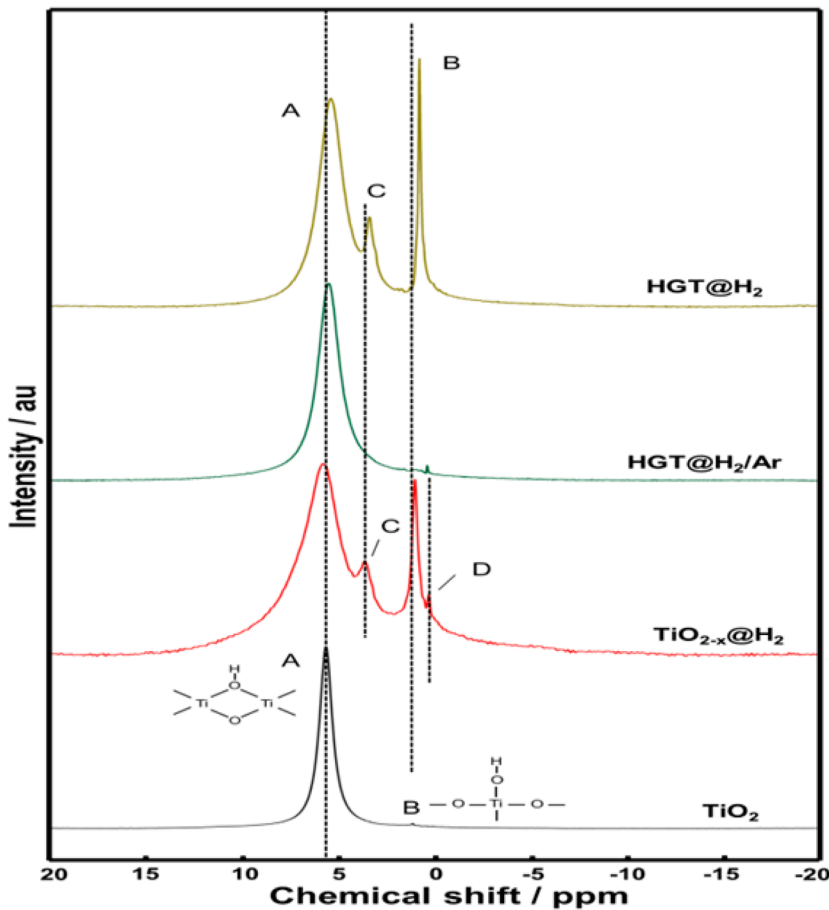


Figure 2. Solid state ^1H NMR, of TiO_2 , $\text{TiO}_{2-\text{x}}@\text{H}_2$, and hydrogenated graphene/ $\text{TiO}_{2-\text{x}}$ composites.

Table 2. ^1H NMR Chemical Shift and XPS Peak Area Ratios of C- and O-Containing Bonds

samples	NMR chemical shifts ^a				XPS C 1s ^b		XPS O 1s ^b	
	A	B	C	D	[C—C/C—H]/C=C	%[C—C/C—H]	O _{II} /O _I	O _{III} /O _I
TiO_2	5.63	1.18	-	-	-	-	0.277	0.182
$\text{TiO}_{2-\text{x}}@\text{H}_2$	5.76	1.04	3.68	0.28	-	-	0.666	0.498
HGT@H ₂ /Ar	5.49	-	-	0.38	0.826	33.92	0.595	0.635
HGT@H ₂	5.35	0.83	3.44	-	1.155	39.74	0.760	0.221

^a ^1H NMR chemical shift. ^bObtained by XPS.

0.83 ppm are recorded for pure H_2 atmosphere. The resonances over HGT composites with upfield shifting due to the higher electronegativity of carbon atoms can be the superposition of an additional carbonaceous component apart from $\text{TiO}_{2-\text{x}}$. The resonance in the range of $\delta = 5.5\text{--}5.8$ ppm can be tentatively assigned to $-\text{CH}$ protons and aromatic protons which arise from carbonaceous species and are essentially immobile as a result of strong interaction with the structure, while the signals at 3.90 and 1.28 ppm can be assigned to the tertiary C—O—H group and aliphatic protons ($-\text{CH}_3$ methyl, $-\text{CH}_2$ methylene).^{60,61} These resonances in HGT composites are most likely overlapping with strong signals of $\text{TiO}_{2-\text{x}}$ due to its minority in mass composition. It is noteworthy that the hydrogenation dramatically reflects the alteration in the hydrogen-bonding network of the materials. Such structural changes upon H_2 reduction environments suggest different behavior in photocatalytic performance of these composite materials.

Morphological Studies—SEM and TEM. The local morphologies of blank and composite materials were investigated by electron microscopy. Typical SEM and TEM images of HGT composites are displayed in Figure 3. Figure 3B clearly shows $\text{TiO}_{2-\text{x}}$ particles well distributed on HG layer in HGT@H₂/Ar. The inversed FFT images identify the fringe disorder along with the lattice expansion, $d_{101} = 0.378$ nm, compared to either TiO_2 or $\text{TiO}_{2-\text{x}}$. As shown in Figure S5 (Supporting Information), well-resolved lattice fringes with interplanar spacings of 0.348 and 0.347 nm are revealed in TiO_2 and $\text{TiO}_{2-\text{x}}$ respectively, corresponding to the d -spacing of the (101) plane of anatase which is consistent with XRD results. It is obvious that the absence of a highly disordered layer at the outer shell of the particles as annealed under pure H_2 is inconsistent with some previous reports.^{41,43} Some part of the image became blurred, and lattice disorder and dislocation occurs instead, as can be seen in the plot profile of lattice fringe in Figure S5C,D. Meanwhile, the existence of few curled layers of HG (3–5 layers, visible interplanar spacing of 0.52 nm)

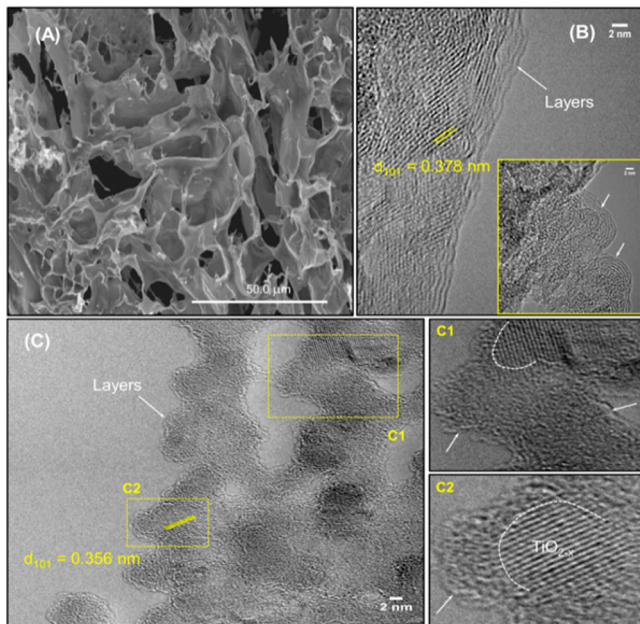


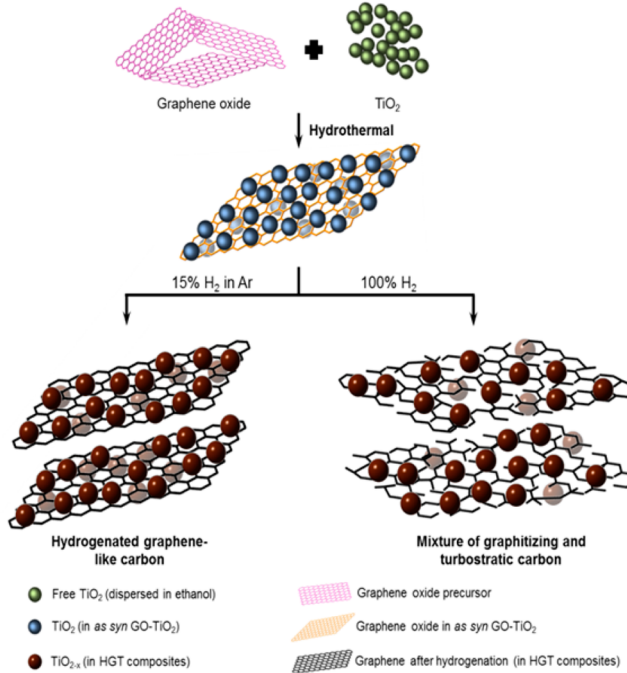
Figure 3. (A) SEM and (B) TEM micrograph of HGT@H₂/Ar and (C) TEM image along with local enlarged images of HGT@H₂. Inset of (B) is the image taken at specific edge showing different geometry of HGT@H₂/Ar.

surrounding TiO_{2-x} particles and highly disordered carbon layers are additionally detected at some specific edges as indicated in the inset of Figure 3B. It can be relevant to the chemical bonding interaction (electrostatic and van der Waals interactions) and intimate interfacial contact between hydroxyl groups on the TiO₂ surface and abundant oxygen-containing functional groups on the basal planes and at the edges of the GO precursor. It is well accepted that, due to such an abundance of these hydrophilic functional groups, GO acts as “a big macromolecular surfactant”, not only well dispersing in aqueous phase but also offering a large quantity of reactive sites to sufficiently interact with TiO₂.¹⁹ Such HG-wrapped TiO_{2-x} structure may be a beneficial factor to the charge transfer and separation from TiO₂ to the carbonaceous layers.

More importantly, such unique geometry is exclusively obtained over HGT composites annealed in high purity H₂ as shown in Figure 3C. The lattice relaxation is also observed in TiO_{2-x} with $d_{101} = 0.356$ nm (also see in Figures S6 and S7 in Supporting Information). Thin layers of HG almost disappear; instead, the highly disordered carbon or turbostratic carbon in a wormhole-like structure is achieved. Turbostratic carbons, the intermediate between the ideal graphite and amorphous carbon materials, are built up by nanoscale imperfect graphite crystallites, arranged almost parallel to one another, but with random orientation.^{62–65} Some regions of turbostratic structure consist of small packets of three-dimensionally (3D) ordered materials with disordering between packets, i.e., the hollow-like central regions surrounded by graphitic layers.⁶³ Similar crystalline-to-amorphous, order-to-disorder transformation and reversed process have been reported where the coexistence of sp²- and sp³-bonded carbon atoms are observed.^{66–68} The presence of highly disordered carbon or turbostratic carbon in the HGT@H₂ composite is coincident with the Raman results where lower I_D/I_G was obtained. The carbonaceous component in terms of either hydrogenated graphene or a mixture of graphitic-like and turbostratic carbon obviously works as a grain

boundary barrier, retarding the growth of anatase grain crystallites and thus leading to diminished crystallite sizes in comparison with TiO₂ and TiO_{2-x} as evident from XRD. Thus, in our study, as illustrated in Scheme 1, in the presence of TiO₂,

Scheme 1. Illustration of Topotactic Transformation from a Hydrogenated Graphene-Like Structure to a Mixture of Graphitizing- and Non-Graphitizing Carbon as Annealing GO/TiO₂ Composite under Different H Atmospheres



the reduction in an H-rich atmosphere results in a topotactic transformation from hydrogenated graphene-like structure to a mixture of graphitizing- and nongraphitizing carbon.

Electronic Properties and Chemical States—XPS Analysis. Further understanding of the electronic and chemical nature of the carbon and TiO_{2-x} in HGT composites was unraveled by means of synchrotron XPS spectroscopy (Figure 4). Core-level Ti 2p and O 1s spectra are measured to gain insight into the surface structure of Ti and O species. As depicted in Figure 4A, two spin-orbital splitting Ti 2p_{3/2} and Ti 2p_{1/2} peaks at 458.4–458.6 and 464.2–464.4 eV in blank and composite materials implicates the Ti⁴⁺ chemical state. The peak broadening might be due to either the interaction between TiO_{2-x} and HG, resulting in Ti–C bonding, or the formation of oxygen vacancy upon hydrogenation (resolved into two peaks at 459.5–460.2 and 465.3–466.0 eV). However, very small features at 457.3–457.5 eV in the fitted spectra for TiO_{2-x}@H₂ and both HGT samples can be attributed to lowering the asymmetrical profile in pristine TiO₂, denoted as (i) oxidation state, Ti³⁺. The existence of Ti³⁺ implicates the generation of oxygen defects in these samples, in particular, oxygen vacancies, to balance the charge compensation. The bonding environment of oxygen is shown in Figure 4B. Three components of oxygen atoms are fitted from crystal lattice oxygen species O²⁻ (O_I, 530.1 eV); (ii) oxygen vacancy defect or surface low-coordinated oxygen ions, i.e., O₂₋, O₂₋²⁻, O⁻, CO₃²⁻ (O_{II}, 531.8 eV); and (iii) hydroxyl-type oxygen species (OH⁻) and surface-adsorbed molecular water (H₂O or O^{δ-}) (O_{III}, 533.0 eV).⁶⁹ It has been acknowledged that the physical

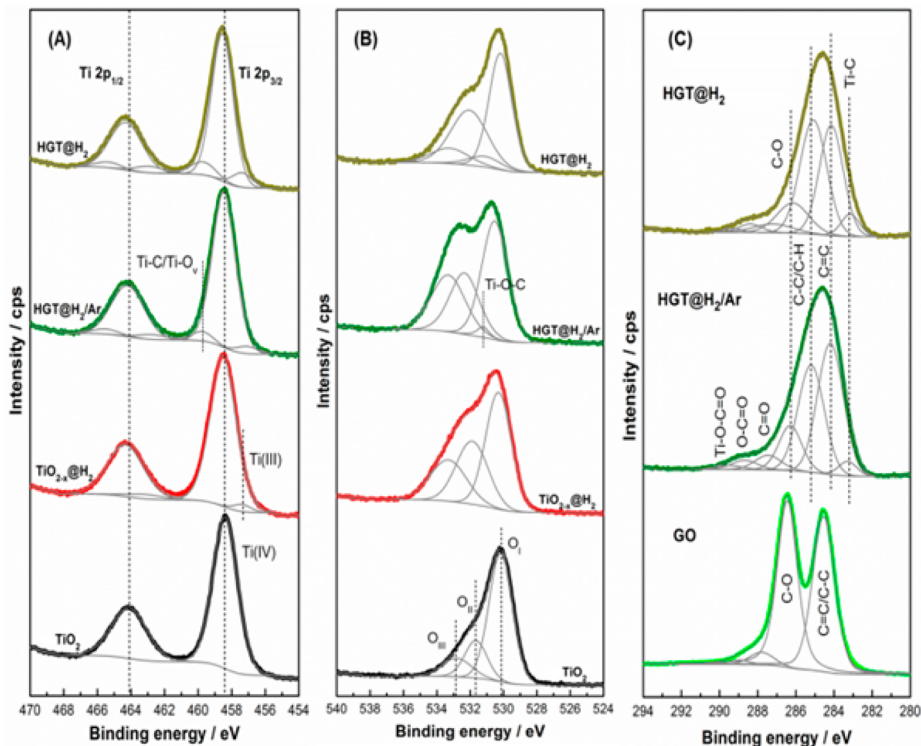


Figure 4. High resolution core-level XPS spectra of TiO_2 , $\text{TiO}_{2-x}\text{@H}_2$, and HGT composites: (A) Ti 2p, (B) O 1s, and (C) C 1s (peak fitting on Shirley backgrounds).

absorbed hydroxyl groups on TiO_2 can be easily removed under ultrahigh vacuum conditions typical of XPS measurements, and the O_{II} and O_{III} peaks can be indeed originated from the species associated with the surface defects or strongly bound to surface defects on TiO_2 . It is clear that the O_{II} and O_{III} features developed with hydrogenation and HG addition, which possibly attributes to the shortage of oxygen in a reducing atmosphere. As summarized in Table 1, the relative ($\text{O}_{\text{II}}/\text{O}_{\text{I}}$) and ($\text{O}_{\text{III}}/\text{O}_{\text{I}}$) area ratios drastically increase from 0.277 to 0.595 and 0.760 for $\text{HGT@H}_2\text{/Ar}$ and HGT@H_2 , respectively, indicating the generation of oxygen defects. Additionally, the small peak located at 531.0–531.2 eV in HGT composites is assignable to $\text{Ti}-\text{O}-\text{C}$ bonding due to the chemical interaction between metal oxide and the carbonaceous material.^{22,30} The peak shift to higher binding energy along with an increment in relative ($\text{O}_{\text{II}}/\text{O}_{\text{I}}$) and ($\text{O}_{\text{III}}/\text{O}_{\text{I}}$) peak area ratios in TiO_{2-x} and HGT composites identifies the hydroxylated or oxyhydroxylated surface, resulting in the introduction of a large amount of negatively charged oxygen vacancies. Similar phenomena can be found in the literature.^{70,71} The presence of these defect sites probably affects the separation of induced electrons/holes and charge transfer, as well as the photocatalytic performance.

The high resolution C 1s spectra in Figure 4C can be deconvoluted into several components, including sp^2 -C bonds of the graphene skeleton ($\text{C}=\text{C}$, 284.2 eV), sp^3 -hybridized carbons ($\text{C}-\text{C/C-H}$, 285.2 eV), alcohol, epoxy, and ether groups ($\text{C}-\text{O}$, 286.3 eV), carbonyl groups ($\text{C}=\text{O}$, 287.5 eV), and carboxylic acid/ester groups ($\text{O}-\text{C}=\text{O}$, 288.8). Compared to the pristine GO, the peak intensities of $\text{C}-\text{O}$, $\text{C}=\text{O}$, and $\text{O}-\text{C}=\text{O}$ substantially diminish, implicating that GO was almost reduced to HG through the hydrothermal and subsequent hydrogenation processes. The larger the amount of residual O-containing functional groups, the lower the conductivity of HG. Interestingly, the sp^3 -bonded C dominates,

occupying 39.74% of the C concentration, as reduced HGT composite in an H-rich atmosphere. As shown in Table 2, the relative area ratio of $\text{C}-\text{C/C-H}$ (sp^3 -carbon) and $\text{C}=\text{C}$ (sp^2 -carbon) strongly increases from 0.826 to 1.155. Our results are in agreement with the literature on hydrogenated graphene, graphone, and graphene.^{39,56} The presence of well-defined C—O bonds after hydrogenation is in agreement with Wang et al.'s computations⁷² that studied the hydrogenation of epoxy on the surface of graphene oxide by H_2 and revealed that it not only converts it into a hydroxyl but also simultaneously transforms an sp^2 carbon to sp^3 carbon. Two features centered at 283.2 and 289.6 eV correspond to $\text{Ti}-\text{O}-\text{C}=\text{O}$ and $\text{Ti}-\text{C}$ due to the strong coupling (covalent interaction) between TiO_{2-x} and HG.^{17,25,30} Especially, the dominance of $\text{Ti}-\text{C}$ bonds (5.43%) in HGT@H_2 clearly indicates the close interconnection between TiO_{2-x} and carbonaceous layers.

Based on TEM, XPS, and Raman spectra, it is plausible to suggest that, in the presence of TiO_2 nanoparticles, GO sheets can undergo a topotactic transformation from graphitic carbon (honeycomb-like structure) to a mixture of graphitic and turbostratic carbon (amorphous/disordered) as altering the calcination atmosphere from a mild to an H-abundant environment. XRD/PDF, NMR, Raman, and XPS results also imply there are remarkable changes in structure and chemical bonding states of TiO_2 , accompanied by the strong electronic communication between 0 and 1D metal oxide and 2D carbon layers upon hydrogenation through the formation of $\text{Ti}-\text{C}/\text{Ti}-\text{O}-\text{C}$ bonds and, thus, an interfacial contact between them. Such differences in textural, structural, and electronic properties possibly impact the migration efficiency of photo-induced electrons, the interfacial electron transfer, and the charge recombination of HGT composites that are strongly relevant to the photocatalytic H_2 -evolution activity.

Photocatalytic H₂ and O₂ Evolution Measurements. Figure 5 compares the H₂ generation performance between

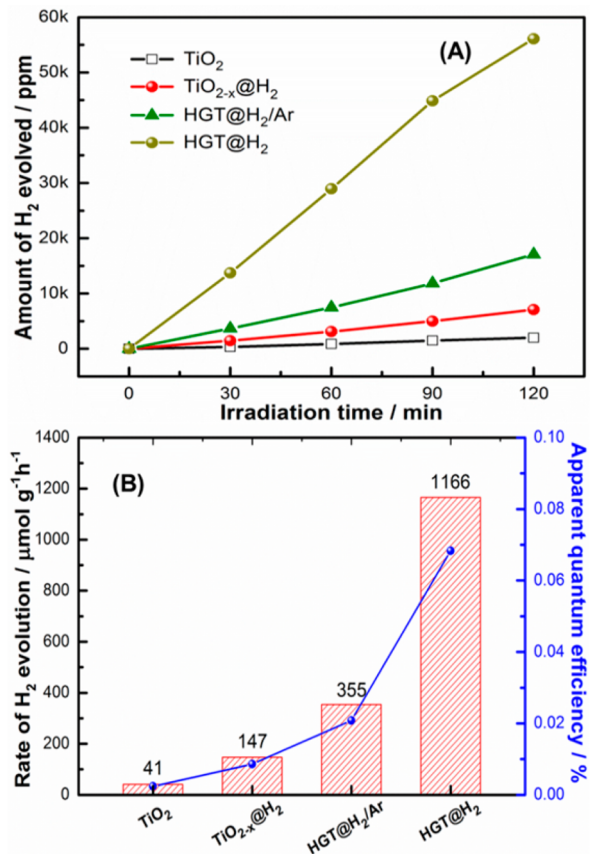


Figure 5. (A) Time curve of H₂ production and (B) mass-normalized evolution rates and quantum efficiencies over TiO₂, TiO_{2-x}@H₂, and hydrogenated graphene/TiO_{2-x} composites, respectively (aqueous methanol 20 vol % as sacrificial agent, 150 W xenon arc lamp equipped with CuSO₄ filter at 293 K, 310 nm < λ < 625 nm).

HGT composites, TiO_{2-x}@H₂ and TiO₂, irradiated by the full output of a Xe lamp equipped with CuSO₄ filter (310 < λ < 625 nm) without the use of a noble metal cocatalyst. The time course of the reaction in Figure 5A shows the proportional increase in the evolved H₂ over time for each sample. It is clear that the presence of HG drastically accelerates the generation of H₂ under UV-visible light. As shown in Figure 5B, the mass specific activity of reduced titania (147 μmol g⁻¹ h⁻¹) is ca. 3.5 times higher than that of air-treated TiO₂ (41 μmol g⁻¹ h⁻¹), possibly arising from the downward shift of the conduction band or the existence of a midgap state that is lower than the reduction potential of H⁺/H₂ by the introduction of defects through hydrogenation.⁴¹ Chen et al.⁴¹ described that the energy distribution of midgap states differed from that of a single defect in a crystal, forming a continuum extending to and overlapping with the conduction band edge (known as band tail states). These band tail states merge with the valence band, extending the energy states. These defects also serve as trapping sites, preventing the charge carriers from the rapid recombination and improving the electron transfer and, hence, the photocatalytic performance. The H₂ evolution rate is further enhanced to 355 μmol g⁻¹ h⁻¹ by the addition of hydrogenated graphene and much greater than commercial TiO₂ P25 (Degussa) as shown in Figure S8 (Supporting Information).

Interestingly, the rate of H₂ production over the HGT@H₂ composite is found to sharply increase to 1.166 mmol g⁻¹ h⁻¹, approximately 7.9 and 3.3 times higher than TiO_{2-x} and HGT composite annealed under 15% H₂ in Ar atmosphere, respectively.

One of the reasonable concerns is whether the HG itself can act as the hydrogen reservoir during hydrogen evolution. Herein, 3 mg of HGT@H₂ generated ~7 μmol (14 μg) of H₂ after 2 h of irradiation. Assuming full coverage of hydrogen on the graphene sheet by hydrogenation in pure H₂ atmosphere, each atomic hydrogen can hypothetically bond to each carbon atom. Thus, the maximum amount of hydrogen “stored” in HGT@H₂ is 2.3 μg. It is noteworthy that, in this study, the gas phase hydrogenation of GO/TiO₂ in the H₂-enriched environment at 20 psi does not produce fully hydrogenated graphane (as proven by XPS and Raman). Both experimental reports and DFT calculations on hydrogenated graphene estimated the hydrogenation efficiency of <10 atom % even under hydrogen plasma.³⁸ Thus, the amount of evolved H₂ during catalysis is much greater than the amount of hydrogen potentially “stored” in the composite. On the basis of these considerations hydrogenated GO support can be safely eliminated as the potential source of hydrogen gas produced during photocatalysis.

The apparent quantum efficiency (QE), which is given by the ratio between the moles per second of hydrogen produced and the moles (einstens) of photons per second,^{73–75} for these materials was also calculated (see detail in Supporting Information). In some studies of photocatalytic water splitting over metal oxides and composite materials, the QE at a specific wavelength (monochromatic radiation) was reported whereas the reaction has been conducted under broadband radiation (polychromatic irradiation).^{17,76,77} Another strategy has been the combination of band-pass and cutoff filters to determine QE over narrow bandwidth or over maxima band.^{78,79} Herein, based on the calculation over the spectral range of 310–625 nm as shown in Figure 5B, 0.068% and 0.021% were obtained for HGT@H₂ and HGT@H₂/Ar composites, much greater than TiO_{2-x} (0.0086%) and TiO₂ (0.0024%). QE of 0.102% was achieved for HGT@H₂ as calculated over the wavelength of 400–625 nm when using both the CuSO₄ and 400 nm long pass filter (see Tables S1 and S2 in Supporting Information).

It is apparent that the reduction in the H₂-rich atmosphere shows a remarkable improvement in photocatalytic performance via the highest hydrogenation extent. Considering several other GR/TiO₂ composites synthesized and reduced by different methods,^{15–30} due to the higher work function, Φ_{GR} = -4.42 eV (vs vacuum) and Φ_{TiO₂} = -4.2 eV^{21,80} GR acts as the electron acceptor and conductor to capture and shuttle photoexcited electrons from the conduction band of TiO₂, efficiently prolonging the lifetime and improving the mobility of electrons (while photogenerated holes are scavenged by the methanol sacrificial agent) and, thus, facilitating H₂ production. The greater separation efficiency of photoinduced electrons/holes and faster charge transfer was additionally proven by the remarkable enhancement in transient photocurrent response over HGT composites compared to TiO₂ and TiO_{2-x}@H₂ (shown in Figure S9, Supporting Information). Herein, it can be inferred that the carbonaceous layers irrespective of hydrogenated graphene or disordered or turbostratic carbon play the identical role as GR. Mixture of graphitizing- and turbostratic carbon enhances the strong interactions and maximizes the intimate interfacial contact between 0D TiO_{2-x}

nano-particles and 2D carbonaceous layers, which favors the interfacial electron transport and efficiently retards the charge recombination. The other factors which may contribute to the enhanced performance will be discussed later.

Numerous studies on GR–TiO₂ composites have reported the crucial role of GR amount in optimizing the photocatalytic performance. Li and Cui²⁸ and Qiu et al.³⁰ reported that the mass ratio of 0.2% exhibited the best H₂ generation efficiency when they increased the carbonaceous content to below 1 wt %. However, Singh et al.²⁴ found that the optimal graphene content was 1 wt %, giving a H₂ evolution of 26 μmol h⁻¹, much greater than that observed in TiO₂. Xiang et al.¹⁷ varied the weight percentages of GR to TiO₂ (0, 0.2, 0.5, 1, 2, and 5 wt %), and the highest H₂-evolved rate was also obtained for the composite containing 1 wt % of graphene, 41 times greater than that of TiO₂ nanosheets. Otherwise, Dubey et al.²⁷ observed that 2 wt % of RGO facilitated the fastest H₂ generation rate, 127.5 μmol cm⁻² h⁻¹, whereas slightly lower activities were obtained as increasing the RGO amount to 5 and 10 wt %. Similarly, Gao et al.²³ found that the optimal H₂ evolved amount, ca. 530 μmol within 120 min, was achieved under deep UV irradiation over the composite containing 2 wt % of sulfonated graphene oxide (SG) as they varied the mass of SG as following: 0.5, 1, 2, 3, and 5 wt %. Lv et al.¹⁸ also concluded that the rate of H₂ production reached the highest value when the content of graphene in the composite was 2 wt %. Zhang et al.¹⁵ obtained the enhancement in H₂ production along with the increase of graphene content from 1 to 5 wt % and then a significant drop with further increasing to 10 wt %. Fan's report¹⁶ elucidated that the amount of H₂ evolved was the largest over the composite composed of 20 wt % of RGO. In addition, several studies have indicated that 1 or 5 wt % of GR showed the best photocatalytic performance toward the selective oxidation of alcohols¹⁹ or pollutant degradation.²² It is obvious that optimizing the loading content of graphene strongly depends on the preparation method and the experimental parameters as well as the specific structure and morphology of the composite materials. An excess graphene might shield the active sites on the surface of the photocatalyst, preventing the incident light penetration and hindering the electron generation, thus suppressing the H₂ production.^{17,18,28} It may increase the opportunity for the collision of electrons and holes, promoting the recombination of the photoinduced charge carriers.¹⁵ In our study, HGT@H₂ composite comprising nominal 1 wt % of HG showed the highest H₂ amount as shown in Figure S10 in Supporting Information.

It has been well established that the noble metal cocatalysts, i.e., Pt, Ru, or Rh, are usually loaded onto the photocatalysts (with 0.5–1 wt %) to facilitate the photocatalytic water splitting performance because they enhance the separation of photo-generated electrons/holes, further improving the photocatalytic activity for proton production and water oxidation. However, tremendous efforts have been made in order to (i) reduce the cocatalyst content, (ii) replace noble metal cocatalyst with other abundant transition metals, and (iii) explore potentially sustainable, cheap, efficient candidates to replace these noble metals, especially Pt, due to its extremely high cost and scarcity. Carbonaceous materials have been considered as promising alternatives to noble metal cocatalysts.^{3–14} Herein, the photoactivity measurement under the presence of 1 wt % Pt cocatalyst was conducted for comparison (Figure 6). Pt nanoparticles were preloaded on *as-syn* TiO₂ by the impregnation method using H₂PtCl₆ as a metal precursor,

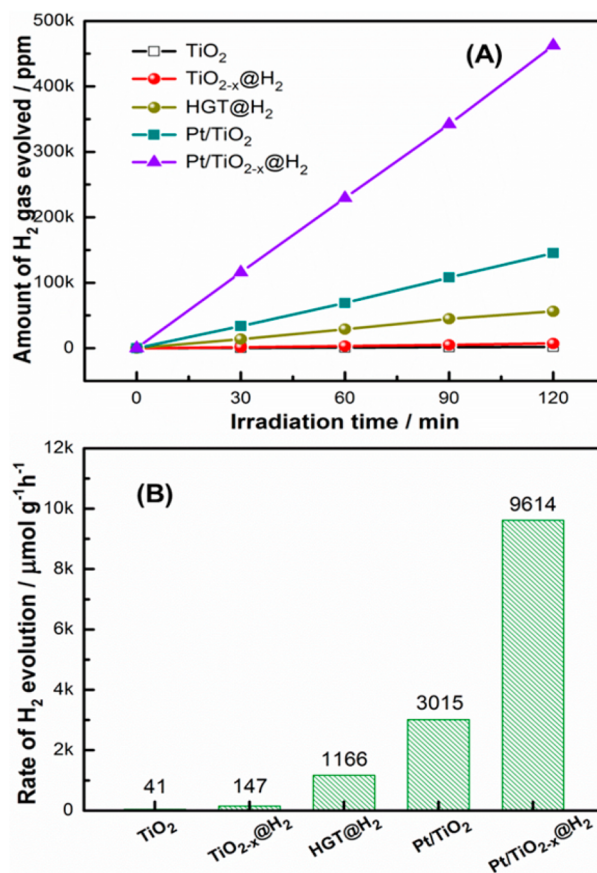


Figure 6. Comparison of H₂ evolution between Pt nanoparticles and hydrogenated graphene cocatalysts on TiO₂ and TiO_{2-x}@H₂ in aqueous methanol solution (150 W xenon arc lamp equipped with CuSO₄ filter at 293 K, 310 nm < λ < 625 nm).

followed by the calcination in either ambient air or high-purity H₂ atmosphere. The time course in Figure 6A shows the enhanced activity of hydrogen production over the samples containing Pt nanoparticles. The H₂ evolution rate achieves 3.015 mmol g⁻¹ h⁻¹ over the Pt/TiO₂ sample as seen in Figure 6B, approximately 73.5-times higher than that for the blank sample (41 μmol g⁻¹ h⁻¹). The rate exceeds 9.614 mmol g⁻¹ h⁻¹ with Pt/TiO₂ samples hydrogenated under a H₂-rich environment. The activity is 3.2-, 65.4-, and 234.5-times of that obtained from Pt/TiO₂, TiO_{2-x}@H₂, and bare TiO₂, respectively. Due to greater work function of Pt (~5.64 eV),⁸¹ the photoinduced electron transfer from the TiO₂ conduction band to Pt is energetically favorable, and the holes are localized within TiO₂, therefore effectively increasing charge carrier separation and then making the electrons accessible for proton reduction to form H₂. It has been reported recently by Zhu et al.⁸² that such superior activity may be attributed to the involvement of hydrogen spillover from Pt to TiO₂ that greatly enhanced the catalytic activity. It is interesting to notice that the H₂ evolution rates of Pt/TiO_{2-x}@H₂ and Pt/TiO₂ are only 8.2- and 2.6-times higher than that of HGT@H₂, respectively, with the same nominal loading amount of GO and Pt (1 wt %). Thus, the highest photocatalytic H₂ evolution performance using an HGT@H₂ composite equivalent to low loading of Pt (~0.12 wt %) simply demonstrates the potential of hydrogenated graphene-based TiO₂ composites to successfully rival the noble-metal-based photocatalysts.

On the other hand, with oxidative half-reaction of overall water splitting, the water oxidation has been acknowledged to be much more challenging than H₂ production due to the consumption of four positive holes to oxidize water to oxygen and more stringent energetic requirements. As shown in Figure 7, the hydrogenated titania creates 439 μmol of O₂ per hour per

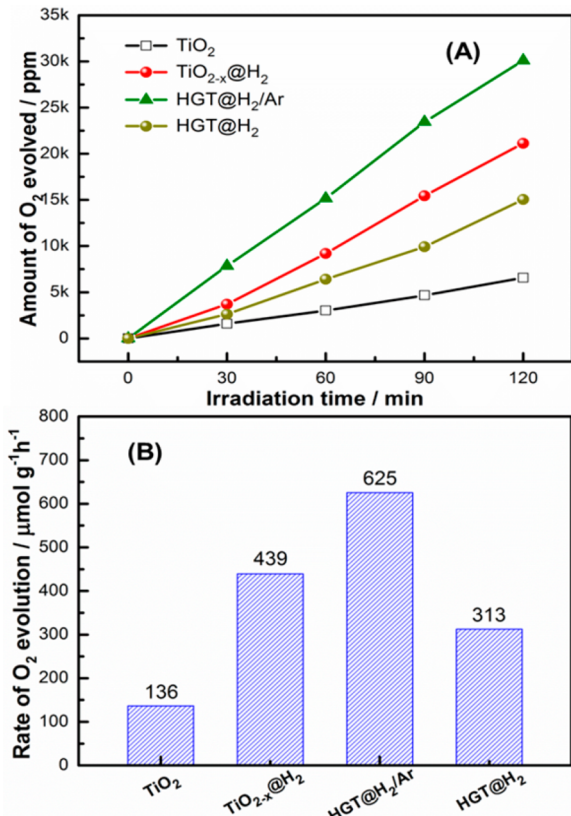


Figure 7. Light-driven O₂ production of TiO₂, TiO_{2-x}@H₂, and HG/TiO_{2-x} composites (aqueous AgNO₃ 0.01 M as sacrificial agent, 150 W xenon arc lamp equipped with CuSO₄ filter at 293 K, 310 nm < λ < 625 nm).

gram of catalyst, which is 3.2-fold higher than that over TiO₂. This enhancement possibly implies that the hydrogenation significantly impacts the valence band structure of TiO₂ where the water oxidation takes place. However, the presence of hydrogenated graphene under H₂/Ar flow slightly enhances the O₂ performance, generating 625 μmol g⁻¹ h⁻¹, whereas post-treatment by pure H₂ makes the composite worse than TiO_{2-x} toward water oxidation (313 μmol g⁻¹ h⁻¹).

Apart from the mass normalization for catalyst effectiveness, it has been known that the normalization of the catalytic activity (i.e., the rate of gas evolution) to photoactive surface sites (such as specific surface area or number of exposed photoactive sites) further provides a better understanding of bulk and surface structural variations due to strong sensitivity to both crystallinity of the bulk lattice and surface features.^{73,83} Figure 8A shows the corresponding BET surface area normalized turnover rate of H₂ and O₂ production. As shown in Table 1, HGT@H₂/Ar possesses a large surface area (>120 m² g⁻¹) which can be attributed to the smaller average crystallite size and the presence of stacked HG layers previously elucidated by XRD and TEM. Consequently, the result clearly indicates the negative effect of the HG additive on O₂

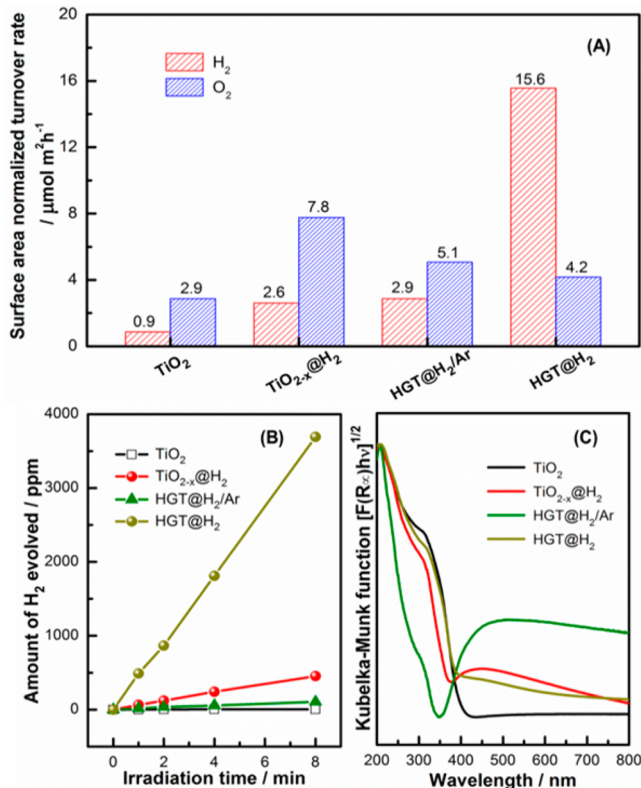


Figure 8. (A) Surface-area-normalized activity of H₂ and O₂ production, (B) visible-light-driven H₂ evolution (150 Xe arc lamp, CuSO₄, and 400 nm cutoff filter, 400 nm < λ < 625 nm), and (C) UV-vis-DRS spectra of blank and composite materials.

production after normalization to surface area. Reduced titania itself exhibits the highest O₂ evolution rate, ~7.8 μmol m² h⁻¹. It is clear that either hydrogenated graphene or a mixture of HG and turbostratic carbon is not an optimal candidate for photocatalytic water oxidation. It can be ascribable to the surface oxygen vacancies which are not stable and even susceptible to oxidation by dissolved oxygen in water; in contrast, the oxygen vacancies in the bulk can avoid the interaction with O₂.⁴⁴ It is proposed that, due to a large concentration of oxygen defects in the HGT composites, the fraction of bulk oxygen vacancies can be much higher than the others, possibly leading to lower O₂ evolution. Otherwise, slightly enhanced H₂ turnover rate of this composite (2.9 μmol m² h⁻¹) is observed compared to hydrogenated titania (2.6 μmol m² h⁻¹). Herein, the highest reactivity is obtained for the HGT composite reduced in a rich-H₂ environment, 15.6 μmol m² h⁻¹.

The photocatalytic H₂ evolution of all samples under visible light irradiation was also studied by using a 400 nm long pass filter (400 < λ < 625 nm). As seen in Figure 8B, compared to blank TiO₂ with no activity, TiO_{2-x}@H₂ produces 454 ppm of H₂ after 8 h of illumination, corresponding to the rate of 2.4 μmol g⁻¹ h⁻¹. HGT@H₂ composite exhibits an increased hydrogen evolution rate of 19.2 μmol g⁻¹ h⁻¹ (generating 3692 ppm of H₂ gas), whereas HGT@H₂/Ar shows much lower activity even compared to reduced titania. Generally, the photocatalytic gas production over HGT composites is strongly affected by the reduction environment, and the diverse photocatalytic performance may be associated with several factors. One of the most important factors is the optical

Table 3. Comparison of Photocatalytic Activity of Different Graphene-Based Catalysts for Hydrogen Generation

photocatalysts	light source	additive/co-catalyst	sacrificial electron donor	rate of H ₂ evolution, μmol g ⁻¹ h ⁻¹	quantum efficiency, %	ref
graphene/TiO ₂	500 W Xe lamp	-5 wt % graphene -no noble-metal-co-catalyst	0.1 M Na ₂ S–0.04 M Na ₂ SO ₃	-UV-visible: 86 -visible: not reported	not reported	15
3D graphene/TiO ₂ hydrogel	300 W Xe lamp 420 nm cutoff filter	-10 wt % graphene -8 wt % Au cocatalyst	10% (v/v) CH ₃ OH–H ₂ O	-UV-visible: 51 (without Au) 242 (with Au) visible: 58 (without Au)	not reported	23
Ag/graphene/P25	Xe lamp	-Five wt % graphene -1.5 wt % Ag cocatalyst	10% (v/v) CH ₃ OH–H ₂ O	-UV-visible: 100 (with Au) 210 (without Ag) 353 (with Ag) -visible: not reported	not reported	25
graphene/TiO ₂ nanosheet	350 W Xe arc lamp	-1 wt % graphene -no noble-metal-co-catalyst	25% (v/v) C ₂ H ₅ OH–H ₂ O	-UV-visible: 736 -visible: not reported	3.1% (at 365 nm–four 3 W–UV LED lamps)	17
reduced graphene oxide/P25	200 W Xe arc lamp	-20 wt % RGO -no noble-metal-co-catalyst	20% (v/v) CH ₃ OH–H ₂ O	-UV-visible: 740 -visible: not reported	not reported	16
Au/graphene/P25	high-pressure 400 W Hg lamp	-1 wt % graphene -2 wt % Au cocatalyst	10% (v/v) CH ₃ OH–H ₂ O	-UV-visible: 1340 (without Au) 12000 (with Au)	not reported	24
Ag/graphene/P25	Xe lamp	-5 wt % graphene -1.5 wt % Ag cocatalyst	10% (v/v) CH ₃ OH–H ₂ O	-UV-visible: 210 (without Ag) 353 (with Ag) -visible: not reported	not reported	25
hydrogenated graphene/TiO _{2-x}	150 W Xe arc lamp equipped with CuSO ₄ filter 400 nm cutoff filter	-1 wt % hydrogenated graphene -no noble-metal-co-catalyst	-1 wt % hydrogenated graphene -no noble-metal-co-catalyst	-UV-visible: 1166 -visible: 19	0.068% (310–625 nm)	this work
Cu/graphene/P25	300 W high pressure Hg lamp	-2 wt % graphene -1.5 wt % Cu as cocatalyst	20% (v/v) CH ₃ OH–H ₂ O 33% (v/v) CH ₃ OH–H ₂ O	-UV-visible: 12500 (without Cu) 65600 (with Cu) -visible: not reported	not reported	18
vacuum-activated graphene/self-doped TiO ₂	300 W Xe arc lamp/400 nm cutoff filter	-2 wt % graphene -0.37 wt % Pt cocatalyst	20% (v/v) CH ₃ OH–H ₂ O	-UV-visible: not reported -visible: 4000	not reported	30

properties of the materials. Figure 8C illustrates the diffuse reflectance UV-vis spectra of TiO_2 , TiO_{2-x} @ H_2 , and HGT composites. In comparison with air-calcined TiO_2 , which only responds under the UV region, the reduced ones are optically absorbing the visible-light region from 380 to 800 nm, along with the blue-shift of the absorption edge. Interestingly, the HGT@ H_2 /Ar composite exhibits unusual optical behavior where the onset is located at 350 nm and a broad, strong absorption up to 800 nm is observed. However, the edge slightly red-shifts as reducing HGT material in pure H_2 , extending the photoresponse into the visible range up to 800 nm (shown in Figure S11, Supporting Information). It implies that annealing the composite materials under different reducing atmospheres induces different photocatalytic reactivity, probably originated from the formation of Ti—C/Ti—O—C bonds due to a strong interaction between TiO_{2-x} and HG which was proven by XPS spectra above. That explains the highest visible-light-driven H_2 evolution over the HGT@ H_2 composite. Indeed, no rational explanation of the blue-shift is explored in this study; nevertheless, as mentioned above, the band gap of graphene can be easily tuned from a small indirect band gap to a wide direct band gap via the manipulation of the hydrogen reduction.³⁴ The UV-vis-DRS spectra of four reference samples, including GO, GO/ TiO_2 , before hydrogenation, and two hydrogenated graphene samples annealed under 15% H_2 /85% Ar and pure H_2 are also shown in Figure S12 (Supporting Information). The characteristic band at 210 nm and a shoulder at 296 nm in dried GO corresponds to $\pi \rightarrow \pi^*$ transitions of aromatic C=C bonds and n $\rightarrow \pi^*$ transitions of C=O bonds, respectively. After H_2 reduction, the spectra of HG samples are distinct from GO owing to both the breakage of the π -bonding network and the elimination of oxygen-containing functional groups. The HGT composites obviously exhibited the shift toward longer wavelength region compared to the materials without TiO_{2-x} . Recently, Zhang et al.⁴⁸ stated that the hydrogenation of RGO- TiO_2 at below 450 °C induced the cathodic photocurrent, which is a p-type photoresponse, whereas hydrogenated temperature higher than 450 °C converted RGO to n-type semiconductor. The formation of p-n heterojunction was suggested, building the inner electric fields at the interfaces between RGO and TiO_2 , significantly increasing the charge separation efficiency.⁴⁸ Briefly, the semiconductor behavior of the composites had a crossover from p-type to n-type when the hydrogenation temperature increased from 450 to 550 °C. There is no doubt that, herein, hydrogenated reduced graphene at 500 °C displays not only the semiconductor behavior but also different interesting properties due to the presence of additional turbostratic carbon. Therefore, the different nature of carbon structures in the composites possibly leads to different optical properties. The coupling between HG and TiO_{2-x} requires further analysis and study to clarify a mechanistic pathway.

It is also worth noting that such differences in photocatalytic performance can be partially ascribed to the introduction of abundant defects and different carbon speciation under different hydrogenation conditions. The hydrogenation-induced oxygen vacancies (as confirmed by XPS analysis) can behave as an electron donor and significantly increase the donor density in TiO_{2-x} , thus possibly improving the charge transport. Similar phenomena have been demonstrated on hydrogenated titania in several previous reports.^{41–43} High separation efficiency of majority and minority carriers due to surface oxygen vacancies and Ti^{3+} centers is an important

factor. The oxygen vacancies work as electron traps while Ti^{3+} sites acts as hole scavengers, both accompanied by the role of adsorption sites where the charge transfer to adsorbed species can prevent the recombination of electron–hole pairs, whereas bulk defects only act as charge carrier traps where electron–holes recombine.⁴⁵ Additionally, the HG can play the role of an electron shuttle, transferring the photogenerated electrons from conduction band of TiO_{2-x} to the HG– TiO_{2-x} interface and eventually to HG conductor, facilitating the separation of electron/hole pairs at the interface and subsequently reducing protons to produce H_2 .^{15–30} Improved performance of hydrogenated composites by ultrahigh-purity H_2 for the light-driven water reduction half-reaction can be attributed to the synergistic effect between the generated defects and emerged graphitic/turbostratic carbon structure which contains more defects and sp^3 -bonded carbon. Such unique structure induces the strong electronic communication between 0D metal oxide and 2D carbon layers through the formation of Ti—C/Ti—O—C bonds, thus, maximizing an intimate interfacial contact between them.^{10,12,13} It also facilitates the interfacial electron transfer rate and the migration efficiency of photoinduced electrons, resulting in superior photocatalytic H_2 -evolution activity.

The comparison of photocatalytic performance of the HGT composite and different catalytic materials reported in the literature using either graphene or noble metal as additives or cocatalysts is shown in Table 3. The rate of H_2 production and quantum efficiency are two important values to evaluate the potential of a photocatalyst. The performance of HGT composites reported in this study is quite impressive compared with the photocatalysts in previous reports. Although, more mechanistic studies are further needed to establish better understanding of photophysical and catalytic properties of the HGT composites, while the findings of the present study provide new insights into the development of the coupling of metal oxides with graphene or graphane to exploit numerous new potential applications.

CONCLUSION

We have investigated the role of hydrogenation on the structure, electronic properties, and photocatalytic activity of hydrogenated graphene/ TiO_{2-x} composites. The hydrogenation not only reduces TiO_2 nanoparticles but also impacts the graphene-like structure in the composites. GO sheets undergo a topotactic transformation from a graphene-like structure to a mixture of graphitic and turbostratic carbon (amorphous/disordered) when altering the calcination atmosphere from a mild to H-abundant environment. The composite annealed upon H-rich conditions exhibits the highest H_2 evolution performance whereas the mild reduction shows a slight improvement in O_2 production. Such enhancement can be attributed to the introduction of a large amount of oxygen vacancies and Ti^{3+} states, retarding the recombination of charge carriers and, thus, facilitating the charge transfer from TiO_{2-x} to the carbonaceous sheet. The findings of the present study may open up an exciting opportunity for developing new strategies for coupling metal oxides with graphene or graphane to replace existing noble metal-based photocatalysts.

■ ASSOCIATED CONTENT

Supporting Information

The Supporting Information is available free of charge on the ACS Publications website at DOI: [10.1021/acs.chemmater.Sb02131](https://doi.org/10.1021/acs.chemmater.Sb02131).

Synthesis procedure of graphene oxide precursor, details for the calculation of apparent quantum efficiency, and 11 supporting figures (Figures S1–S11) of lamp irradiance spectra, HR-TEM, PDF, TGA, photocurrent response, plot of Kubelka–Munk function vs photon energy, UV-vis–DRS, and photocatalytic activity comparison (PDF)

■ AUTHOR INFORMATION

Corresponding Author

*(J.A.R.) E-mail: rodriguez@bnl.gov.

Notes

The authors declare no competing financial interest.

■ ACKNOWLEDGMENTS

The research carried out in this manuscript was performed at Brookhaven National Laboratory, supported by the U.S. Department of Energy, Office of Science, Office of Basic Energy Sciences, and Catalysis Science Program under Contract No. DE-SC0012704. This work used resources of the National Synchrotron Light Source (NSLS) and the Center for Functional Nanomaterials (CFN), which are DOE Office of Science User Facilities. We would like to thank Dr. Viet Hung Pham (CFN) for graphene oxide supply and Raman and TGA analyses.

■ REFERENCES

- (1) Novoselov, K. S.; Geim, A. K.; Morozov, S. V.; Jiang, D.; Zhang, Y.; Dubonos, S. V.; Grigorieva, I. V.; Firsov, A. A. Electric Field Effect in Atomically Thin Carbon Films. *Science* **2004**, *306*, 666–669.
- (2) Geim, A. K.; Novoselov, K. S. The Rise of Graphene. *Nat. Mater.* **2007**, *6*, 183–191.
- (3) Singh, V.; Joung, D.; Zhai, L.; Das, S.; Khondaker, S. I.; Seal, S. Graphene based Materials: Past, Present and Future. *Prog. Mater. Sci.* **2011**, *56*, 1178–1271.
- (4) Wu, Z.-S.; Zhou, G.; Yin, L.-C.; Ren, W.; Li, F.; Cheng, H.-M. Graphene/Metal Oxide Composite Electrode Materials for Energy Storage. *Nano Energy* **2012**, *1*, 107–131.
- (5) Xiang, Q.; Yu, J.; Jaroniec, M. Graphene-Based Semiconductor Photocatalysts. *Chem. Soc. Rev.* **2012**, *41*, 782–796.
- (6) Zhang, N.; Zhang, Y.; Xu, Y.-J. Recent Progress on Graphene-Based Photocatalysts: Current Status and Future Perspectives. *Nanoscale* **2012**, *4*, 5792–5813.
- (7) Wang, S.; Sun, H.; Ang, H. M.; Tadé, M. O. Adsorptive Remediation of Environmental Pollutants using Novel Graphene-based Nanomaterials. *Chem. Eng. J.* **2013**, *226*, 336–347.
- (8) Lightcap, I. V.; Kamat, P. V. Graphitic Design: Prospects of Graphene-Based Nanocomposites for Solar Energy Conversion, Storage, and Sensing. *Acc. Chem. Res.* **2013**, *46*, 2235–2243.
- (9) Xiang, Q.; Yu, J. Graphene-Based Photocatalysts for Hydrogen Generation. *J. Phys. Chem. Lett.* **2013**, *4*, 753–759.
- (10) Yang, M.-Q.; Xu, Y.-J. Selective Photoredox using Graphene-Based Composite Photocatalysts. *Phys. Chem. Chem. Phys.* **2013**, *15*, 19102–19118.
- (11) Chowdhury, S.; Balasubramanian, R. Recent Advances in the Use of Graphene-family Nanoabsorbents for Removal of Toxic Pollutants from Wastewater. *Adv. Colloid Interface Sci.* **2014**, *204*, 35–56.
- (12) Yang, M.-Q.; Zhang, N.; Pagliaro, M.; Xu, Y.-J. Artificial Photosynthesis over Graphene–Semiconductor Composites. Are We Getting Better? *Chem. Soc. Rev.* **2014**, *43*, 8240–8254.
- (13) Xiang, Q.; Cheng, B.; Yu, J. Graphene-Based Photocatalysts for Solar Fuel Generation. *Angew. Chem., Int. Ed.* **2015**, DOI: [10.1002/anie.201411096](https://doi.org/10.1002/anie.201411096).
- (14) Li, X.; Yu, J.; Low, J.; Fang, Y.; Xiao, J.; Chen, X. Engineering Heterogeneous Semiconductors for Solar Water Splitting. *J. Mater. Chem. A* **2015**, *3*, 2485–2534.
- (15) Zhang, X.-Y.; Li, H.-P.; Cui, X.-L.; Lin, Y. Graphene/TiO₂ Nanocomposites: Synthesis, Characterization and Application in Hydrogen Evolution from Water Photocatalytic splitting. *J. Mater. Chem.* **2010**, *20*, 2801–2806.
- (16) Fan, W.; Lai, Q.; Zhang, Q.; Wang, Y. Nanocomposites of TiO₂ and Reduced Graphene Oxide as Efficient Photocatalysts for Hydrogen Evolution. *J. Phys. Chem. C* **2011**, *115*, 10694–10701.
- (17) Xiang, Q.; Yu, J.; Jaroniec, M. Enhanced Photocatalytic H₂-production Activity of Graphene-modified Titania Nanosheets. *Nanoscale* **2011**, *3*, 3670–3678.
- (18) Lv, X.-J.; Zhou, S.-X.; Zhang, C.; Chang, H.-X.; Chen, Y.; Fu, W.-F. Synergetic Effect of Cu and Graphene as Cocatalyst on TiO₂ for Enhanced Photocatalytic Hydrogen Evolution from Solar Water Splitting. *J. Mater. Chem.* **2012**, *22*, 18542–18549.
- (19) Zhang, Y.; Zhang, N.; Tang, Z.-R.; Xu, Y.-J. Improving the Photocatalytic Performance of Graphene–TiO₂ Nanocomposites via a Combined Strategy of Decreasing Defects of Graphene and Increasing Interfacial Contact. *Phys. Chem. Chem. Phys.* **2012**, *14*, 9167–9175.
- (20) Sun, L.; Zhao, Z.; Zhou, Y.; Liu, L. Anatase TiO₂ Nanocrystals with Exposed {001} Facets on Graphene Sheets via Molecular Grafting for Enhanced Photocatalytic Activity. *Nanoscale* **2012**, *4*, 613–620.
- (21) Morales-Torres, S.; Pastrana-Martínez, L. M.; Figueiredo, J. L.; Faria, J. L.; Silva, A. M. T. Design of Graphene-based TiO₂ Photocatalysts—a Review. *Environ. Sci. Pollut. Res.* **2012**, *19*, 3676–3687.
- (22) Lu, T.; Zhang, R.; Hu, C.; Chen, F.; Duo, S.; Hu, Q. TiO₂–Graphene Composites with Exposed {001} Facets Produced by a One-pot Solvothermal Approach for High Performance Photocatalyst. *Phys. Chem. Chem. Phys.* **2013**, *15*, 12963–12970.
- (23) Gao, M.; Peh, C. K. N.; Ong, W. L.; Ho, G. W. Green Chemistry Synthesis of a Nanocomposites Graphene Hydrogel with Three-dimensional Nanomesopores for Photocatalytic H₂ Production. *RSC Adv.* **2013**, *3*, 13169–13177.
- (24) Singh, G. P.; Shrestha, K. M.; Nepal, A.; Klabunde, K. J.; Sorensen, C. M. Graphene Supported Plasmonic Photocatalyst for Hydrogen Evolution in Photocatalytic Water Splitting. *Nanotechnology* **2014**, *25*, 265701.
- (25) Yang, Y.; Liu, E.; Dai, H.; Kang, L.; Wu, H.; Fan, J.; Hu, X.; Liu, H. Photocatalytic Activity of Ag-TiO₂-Graphene Ternary Nanocomposites and Application in Hydrogen Evolution by Water Splitting. *Int. J. Hydrogen Energy* **2014**, *39*, 7664–7671.
- (26) Gu, Y.; Xing, M.; Zhang, J. Synthesis and Photocatalytic Activity of Graphene Based Doped TiO₂ Nanocomposites. *Appl. Surf. Sci.* **2014**, *319*, 8–15.
- (27) Dubey, P. K.; Tripathi, P.; Tiwari, R. S.; Sinha, A. S. K.; Srivastava, O. N. Synthesis of Reduced Graphene Oxide–TiO₂ Nanoparticle Composite Systems and Its Application in Hydrogen Production. *Int. J. Hydrogen Energy* **2014**, *39*, 16282–16292.
- (28) Li, H.; Cui, X. A Hydrothermal Route for Constructing Reduced Graphene Oxide/TiO₂ Nanocomposites: Enhanced Photocatalytic Activity for Hydrogen Evolution. *Int. J. Hydrogen Energy* **2014**, *39*, 19877–19886.
- (29) Gao, P.; Sun, D. D. Hierarchical Sulfonated Graphene Oxide–TiO₂ Composites for Highly Efficient Hydrogen Production with a Wide pH Range. *Appl. Catal., B* **2014**, *147*, 888–896.
- (30) Qiu, B.; Zhou, Y.; Ma, Y.; Yang, X.; Sheng, W.; Xing, M.; Zhang, J. Facile Synthesis of the Ti³⁺ Self-doped TiO₂-Graphene Nanosheet Composites with Enhanced Photocatalysis. *Sci. Rep.* **2015**, *5*, 8591.

- (31) Chen, X.; Mao, S. S. Titanium Dioxide Nanomaterials: Synthesis, Properties, Modifications, and Applications. *Chem. Rev.* **2007**, *107*, 2891–2959.
- (32) Muñoz-Batista, M. J.; Kubacka, A.; Fernández-García, M. Effective Enhancement of TiO_2 Photocatalysis by Synergistic Interaction of Surface Species: From Promoters to Co-catalysts. *ACS Catal.* **2014**, *4*, 4277–4288.
- (33) Elias, D. D.; Nair, R. R.; Mohiuddin, T. M. G.; Morozov, S. V.; Blake, P.; Halsall, M. P.; Ferrari, A. C.; Boukhvalov, D. W.; Katnelson, M. I.; Geim, A. K.; Novoselov, K. S. Control of Graphene's Properties by Reversible Hydrogenation: Evidence for Graphane. *Science* **2009**, *323*, 610–613.
- (34) Zhou, J.; Wang, Q.; Sun, Q.; Chen, X. S.; Kawazoe, Y.; Jena, P. Ferromagnetism in Semihydrogenated Graphene Sheet. *Nano Lett.* **2009**, *9*, 3867–3870.
- (35) Cadelano, E.; Palla, P. L.; Giordano, S.; Colombo, L. Elastic Properties of Hydrogenated Graphene. *Phys. Rev. B: Condens. Matter Mater. Phys.* **2010**, *82*, 235414.
- (36) Sun, Z.; Pint, C. L.; Marcano, D. C.; Zhang, C.; Yao, J.; Ruan, G.; Yan, Z.; Zhu, Y.; Hauge, R. H.; Tour, J. M. Towards Hybrid Superlattices in Graphene. *Nat. Commun.* **2011**, *2*, 559.
- (37) Shkrebtii, A. I.; Heritage, E.; McNelles, P.; Cabellos, J. L.; Mendoza, B. S. Graphene and Graphane Functionalization with Hydrogen: Electronic and Optical Signatures. *Phys. Status Solidi C* **2012**, *9*, 1378–1383.
- (38) Pumera, M.; Wong, C. H. A. Graphane and Hydrogenated Graphene. *Chem. Soc. Rev.* **2013**, *42*, 5987–5995.
- (39) Rajasekaran, S.; Abild-Pedersen, F.; Ogasawara, H.; Nilsson, A.; Kaya, S. Interlayer Carbon Bond Formation Induced by Hydrogen Adsorption in Few-Layer Supported Graphene. *Phys. Rev. Lett.* **2013**, *111*, 085503.
- (40) Sofer, Z.; Jankovský, O.; Šimek, P.; Soferová, L.; Sedmidubský, D.; Pumera, M. Highly Hydrogenated Graphene via Active Hydrogen Reduction of Graphene Oxide in the Aqueous Phase at Room Temperature. *Nanoscale* **2014**, *6*, 2153–2160.
- (41) Chen, X.; Liu, L.; Yu, P. Y.; Mao, S. S. Increasing Solar Absorption for Photocatalysis with Black Hydrogenated Titanium Dioxide Nanocrystals. *Science* **2011**, *331*, 746–750.
- (42) Jiang, X.; Zhang, Y.; Jiang, J.; Rong, Y.; Wang, Y.; Wu, Y.; Pan, C. Characterization of Oxygen Vacancy Associates within Hydrogenated TiO_2 : A Positron Annihilation Study. *J. Phys. Chem. C* **2012**, *116*, 22619–22624.
- (43) Chen, X.; Liu, L.; Liu, Z.; Marcus, M. A.; Wang, W.-C.; Oyler, N. A.; Grass, M. E.; Mao, B.; Glans, P.-A.; Yu, P. Y.; Guo, J.; Mao, S. S. Properties of Disorder-Engineered Black Titanium Dioxide Nanoparticles through Hydrogenation. *Sci. Rep.* **2013**, *3*, 1510.
- (44) Li, G.; Lian, Z.; Li, X.; Xu, Y.; Wang, W.; Zhang, D.; Tian, F.; Li, H. Ionothermal Synthesis of Black Ti^{3+} -doped Single-crystal TiO_2 as an Active Photocatalyst for Pollutant Degradation and H_2 Generation. *J. Mater. Chem. A* **2015**, *3*, 3748–3756.
- (45) Pan, X.; Yang, M.-Q.; Fu, X.; Zhang, N.; Xu, Y.-J. Defective TiO_2 with Oxygen Vacancies: Synthesis, Properties and Photocatalytic Applications. *Nanoscale* **2013**, *5*, 3601–3614.
- (46) Su, J.; Zou, X.; Chen, J.-S. Self-modification of Titanium Dioxide Materials by Ti^{3+} and/or Oxygen Vacancies: New Insights into Defect Chemistry of Metal Oxides. *RSC Adv.* **2014**, *4*, 13979–13988.
- (47) Wang, J.; Shen, L.; Nie, P.; Xu, G.; Ding, B.; Fang, S.; Dou, H.; Zhang, X. Synthesis of Hydrogenated TiO_2 -Reduced-Graphene Oxide Nanocomposites and their Application in High Rate Lithium Ion Batteries. *J. Mater. Chem. A* **2014**, *2*, 9150–9155.
- (48) Zhang, X.; Chen, Z. The Enhanced Photoactivity of Hydrogenated TiO_2 @Reduced Graphene Oxide with p-n Junctions. *RSC Adv.* **2015**, *5*, 26328–26334.
- (49) Luo, S.; Nguyen-Phan, T.-D.; Johnston-Peck, A. C.; Barrio, L.; Sallis, S.; Arena, D. A.; Kundu, S.; Xu, W.; Piper, L. F. J.; Stach, E. A.; Polyansky, D. E.; Fujita, E.; Rodriguez, J. A.; Senanayake, S. D. Hierarchical Heterogeneity at the CeO_x - TiO_2 Interface: Electronic and Geometric Structural Influence on the Photocatalytic Activity of Oxide on Oxide Nanostructures. *J. Phys. Chem. C* **2015**, *119*, 2669–2679.
- (50) Muscat, J.; Swamy, V.; Harrison, N. M. First-principles Calculations of the Phase Stability of TiO_2 . *Phys. Rev. B: Condens. Matter Mater. Phys.* **2002**, *65*, 224112.
- (51) Yu, P. Y.; Cardona, M. *Fundamentals of Semiconductors: Physics and Materials Properties*, 4th ed.; Springer: Heidelberg, 2010.
- (52) Sahoo, S.; Arora, A. K.; Sridharan, V. Raman Line Shapes of Optical Phonons of Different Symmetries in Anatase TiO_2 Nanocrystals. *J. Phys. Chem. C* **2009**, *113*, 16927–16933.
- (53) Zheng, Z.; Huang, B.; Lu, J.; Wang, Z.; Qin, X.; Zhang, X.; Dai, Y.; Whangbo, M.-H. Hydrogenated Titania: Synergy of Surface Modification and Morphology Improvement for Enhanced Photocatalytic Activity. *Chem. Commun.* **2012**, *48*, 5733–5735.
- (54) Ferrari, A. C.; Meyer, J. C.; Scardaci, V.; Casiraghi, C.; Lazzeri, M.; Mauri, F.; Piscanec, S.; Jiang, D.; Novoselov, K. S.; Roth, S.; Geim, A. K. Raman Spectrum of Graphene and Graphene Layers. *Phys. Rev. Lett.* **2006**, *97*, 187401.
- (55) Ai, K.; Liu, Y.; Lu, L.; Cheng, X.; Huo, L. A Novel Strategy for Making Soluble Reduced Graphene Oxide Sheets Cheaply by Adopting an Endogenous Reducing Agent. *J. Mater. Chem.* **2011**, *21*, 3365–3370.
- (56) Li, Y.; Chen, H.; Voo, L. Y.; Ji, J.; Zhang, G.; Zhang, G.; Zhang, F.; Fan, X. Synthesis of Partially Hydrogenated Graphene and Brominated Graphene. *J. Mater. Chem.* **2012**, *22*, 15021–15024.
- (57) Crocker, M.; Herold, R. H. M.; Wilson, A. E.; Mackay, M.; Emeis, C. A.; Hoogendoorn, A. M. ^1H NMR Spectroscopy of Titania. Chemical Shift Assignments for Hydroxy Groups in Crystalline and Amorphous Forms of TiO_2 . *J. Chem. Soc., Faraday Trans.* **1996**, *92*, 2791–2798.
- (58) Chary, K. V. R.; Bhaskar, T.; Kishan, G.; Vijayakumar, V. Characterization of $\text{MoO}_3/\text{TiO}_2$ (Anatase) Catalysts by ESR, ^1H MAS NMR, and Oxygen Chemisorption. *J. Phys. Chem. B* **1998**, *102*, 3936–3940.
- (59) Jonsen, P. Identification of Different Hydrogen-Reduced Titania Crystallographic Forms by ^1H NMR Spectroscopy. *Catal. Lett.* **1989**, *2*, 345–350.
- (60) He, H.; Riedl, T.; Lerf, A.; Klinowski, J. Solid-State NMR Studies of the Structure of Graphite Oxide. *J. Phys. Chem.* **1996**, *100*, 19954–19958.
- (61) Ou, B.; Zhou, Z.; Liu, Q.; Liao, B.; Yi, S.; Ou, Y.; Zhang, X.; Li, D. Covalent Functionalization of Graphene with Poly(methyl methacrylate) by Atom Transfer Radical Polymerization at Room Temperature. *Polym. Chem.* **2012**, *3*, 2768–2775.
- (62) Warren, B. E. X-Ray Diffraction in Random Layer Lattices. *Phys. Rev.* **1941**, *59*, 693–698.
- (63) Badami, D. V.; Kaye, G. The Nature of Turbostratic Carbon. *Carbon* **1964**, *1*, 375–375.
- (64) Dasgupta, K.; Sathiyamoorthy, D. Disordered Carbon—Its Preparation, Structure, and Characterization. *Mater. Sci. Technol.* **2003**, *19*, 995–1002.
- (65) Li, Z. Q.; Lu, C. J.; Xia, Z. P.; Zhou, Y.; Luo, Z. X-ray Diffraction Patterns of Graphite and Turbostratic Carbon. *Carbon* **2007**, *45*, 1686–1695.
- (66) Shen, T. D.; Ge, W. Q.; Wang, K. Y.; Quan, M. X.; Wang, J. T.; Wei, W. D.; Koch, C. C. Structural Disorder and Phase Transformation in Graphite Produced by Ball Milling. *Nanostruct. Mater.* **1996**, *7*, 393–399.
- (67) Huang, J. Y. HRTEM and EELS Studies of Defects Structure and Amorphous-like Graphite Induced by Ball-Milling. *Acta Mater.* **1999**, *47*, 1801–1808.
- (68) Barreiro, A.; Börrnert, F.; Avdoshenko, S. M.; Rellinghaus, B.; Cuniberti, G.; Rümmeli, M. H.; Vandersypen, L. M. K. Understanding the Catalyst-free Transformation of Amorphous Carbon into Graphene by Current-induced Annealing. *Sci. Rep.* **2013**, *3*, 1115.
- (69) Dupin, J.-C.; Gonbeau, D.; Vinatier, P.; Levasseur, A. Systematic XPS Studies of Metal Oxides, Hydroxides and Peroxides. *Phys. Chem. Chem. Phys.* **2000**, *2*, 1319–1324.

- (70) Naeem, M.; Hasanain, S. K.; Kobayashi, M.; Ishida, Y.; Fujimori, A.; Buzby, S.; Shah, S. I. Effect of Reducing Atmosphere on the Magnetism of $Zn_{1-x}Co_xO$ Nanoparticles. *Nanotechnology* **2006**, *17*, 2675–2680.
- (71) Mohanty, P.; Mishra, N. C.; Choudhary, R. J.; Banerjee, A.; Shripathi, T.; Lalla, N. P.; Annapoorni, S.; Rath, C. Oxygen Vacancy Induced Phase Formation and Room Temperature Ferromagnetism in Undoped and Co-doped TiO_2 Thin Films. *J. Phys. D: Appl. Phys.* **2012**, *45*, 325301.
- (72) Wang, L.; Lee, K.; Sun, Y.-Y.; Lucking, M.; Chen, Z.; Zhao, J. J.; Zhang, S. B. Graphene Oxide as an Ideal Substrate for Hydrogen Storage. *ACS Nano* **2009**, *3*, 2995–3000.
- (73) Braslavsky, S. E.; Braun, A. M.; Cassano, A. E.; Emeline, A. V.; Litter, M. I.; Palmisano, L.; Parmon, V. N.; Serpone, N. Glossary of Terms Used in Photocatalysis and Radiation Catalysis (IUPAC Recommendations 2011). *Pure Appl. Chem.* **2011**, *83*, 931–1014.
- (74) Serpone, N.; Salinaro, A. Terminology, Relative Photonic Efficiencies and Quantum Yields in Heterogeneous Photocatalysis. Part I: Suggested Protocol (Technical Report). *Pure Appl. Chem.* **1999**, *71*, 303–320.
- (75) Salinaro, A.; Emeline, A. V.; Zhao, J.; Hidaka, H.; Ryabchuk, V. K.; Serpone, N. Terminology, Relative Photonic Efficiencies and Quantum Yields in Heterogeneous Photocatalysis. Part II: Experimental Determination of Quantum Yields (Technical Report). *Pure Appl. Chem.* **1999**, *71*, 321–335.
- (76) Li, Q.; Guo, B.; Yu, J.; Ran, J.; Zhang, B.; Yan, H.; Gong, J. R. Highly Efficient Visible-Light-Driven Photocatalytic Hydrogen Production of CdS-Cluster-Decorated Graphene Nanosheets. *J. Am. Chem. Soc.* **2011**, *133*, 10878–10884.
- (77) Yu, J.; Yang, B.; Cheng, B. Noble-metal-free Carbon Nanotube- $Cd_{0.1}Zn_{0.9}S$ Composites for High Visible-Light Photocatalytic H_2 -Production Performance. *Nanoscale* **2012**, *4*, 2670–2677.
- (78) Zhang, J.; He, R.; Liu, X. Efficient Visible Light Driven Photocatalytic Hydrogen Production from Water using Attapulgite Clay Sensitized by CdS Nanoparticles. *Nanotechnology* **2013**, *24*, 505401.
- (79) Bhunia, M. K.; Yamauchi, K.; Takanabe, K. Harvesting Solar Light with Crystalline Carbon Nitrides for Efficient Photocatalytic Hydrogen Evolution. *Angew. Chem., Int. Ed.* **2014**, *53*, 11001–11005.
- (80) Grätzel, M. Photoelectrochemical Cells. *Nature* **2001**, *414*, 338–344.
- (81) Lide, D. R., Ed. *CRC Handbook of Chemistry and Physics*, 90th ed.; CRC Press: Boca Raton, FL, 2009.
- (82) Zhu, Y.; Liu, D.; Meng, M. H_2 Spillover Enhanced Hydrogenation Capability of TiO_2 Used for Photocatalytic Splitting of Water: A Traditional Phenomenon for New Applications. *Chem. Commun.* **2014**, *50*, 6049–6051.
- (83) Wachs, I. E.; Phivilay, S. P.; Roberts, C. A. Reporting of Reactivity for Heterogeneous Photocatalysis. *ACS Catal.* **2013**, *3*, 2606–2611.